Article

Bottom-up Assembly of Nanoporous Graphene with Emergent Electronic States

Peter H. Jacobse,[⊥] Ryan D. McCurdy,[⊥] Jingwei Jiang,[⊥] Daniel J. Rizzo, Gregory Veber, Paul Butler, Rafał Zuzak, Steven G. Louie,* Felix R. Fischer,* and Michael F. Crommie*

Cite This: *J. Am. Chem. Soc.* 2020, 142, 13507−13514

Read Online

ACCESS | Metrics & More | Article Recommendations | Supporting Information

ABSTRACT: The incorporation of nanoscale pores into a sheet of graphene allows it to switch from an impermeable semimetal to a semiconducting nanosieve. Nanoporous graphenes are desirable for applications ranging from high-performance semiconductor device channels to atomically thin molecular sieve membranes, and their performance is highly dependent on the periodicity and reproducibility of pores at the atomic level. Achieving precise nanopore topologies in graphene using top-down lithographic approaches has proven to be challenging due to poor structural control at the atomic level. Alternatively, atomically precise nanometer-sized pores can be fabricated via lateral fusion of bottom-up synthesized graphene nanoribbons. This technique, however, typically requires an additional high temperature cross-coupling step following the nanoribbon formation that inherently yields poor lateral conjugation, resulting in 2D materials that are weakly connected both mechanically and electronically. Here, we demonstrate a novel bottom-up approach for forming fully conjugated nanoporous graphene through a single, mild annealing step following the initial polymer formation. We find emergent interface-localized electronic states within the bulk band gap of the graphene nanoribbon that hybridize to yield a dispersive two-dimensional low-energy band of states. We show that this low-energy band can be rationalized in terms of edge states of the constituent single-strand nanoribbons. The localization of these 2D states around pores makes this material particularly attractive for applications requiring electronically sensitive molecular sieves.
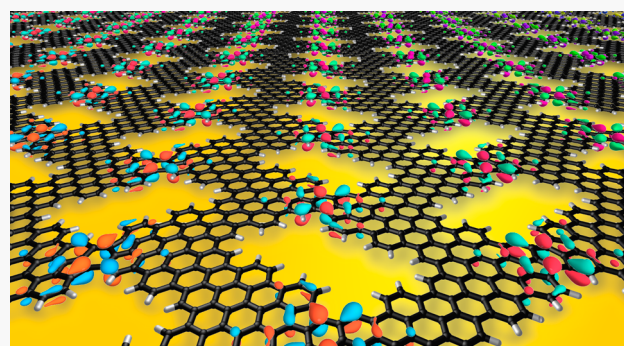
INTRODUCTION

Nanoporous graphene (NPG) is unique in that it exhibits both electronic functionality as a tunable semiconductor and mechanical functionality as a tunable molecular filter membrane. Combining these properties into a single atomically thin, mechanically robust platform makes NPG an excellent candidate for electronically active nanosieve applications such as sequencing, sensing, ion transport, gas separation, and water purification.[1−10] The utility of this material, however, hinges on the ability to induce periodic, atomically precise nanopores and to tailor their precise dimensions and electronic properties. Top-down methods have so far been limited in this regard because they typically produce random, imprecise pores within a material that remains semimetallic.[1,3,5] By contrast, bottom-up approaches offer atomic precision in NPG synthesis through rational design of molecular precursors.[11,12] This has been demonstrated recently through cross-dehydrogenative coupling of bottom-up synthesized graphene nanoribbons (GNRs) featuring periodic bay regions along the edges.[11−14] A disadvantage of the few reported bottom-up synthesized NPGs fabricated in this way is that the constituent nanoribbons are wide gap

semiconductors. Electronic coupling upon lateral extension results in, at most, a modest decrease in the overall band gap compared to that of the constituent one-dimensional (1D) ribbons. In addition, the linkages between ribbons up to now are unable to host low-energy frontier states around the pores as required for possible electronic sieving applications.
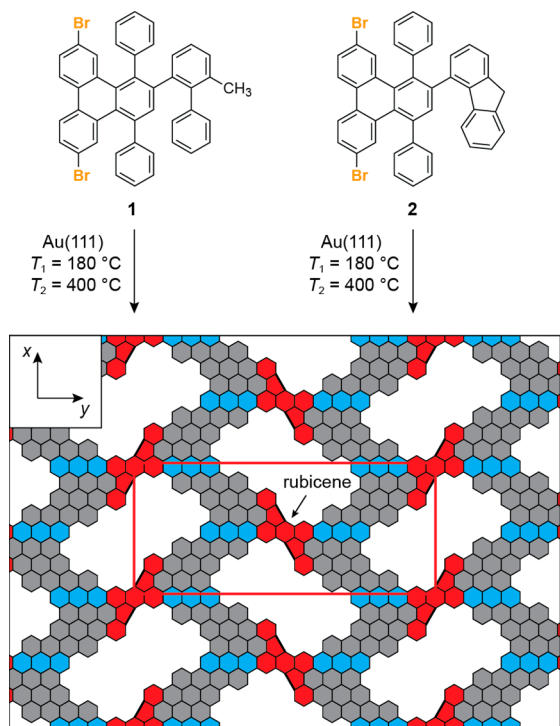
Here, we present a surface-mediated approach to creating NPG by utilizing a novel cross-linking handle that yields a fully conjugated linkage between constituent nanoribbons and results in a new low-energy band of extended states but with much of their wave functions localized along the periphery of the pores. We designed two molecular precursors (**1** and **2** in Scheme 1) functionalized with thermally labile methyl and methylene groups that serve as cross-linking handles. The respective C−H bond dissociation energies (BDE) are similar
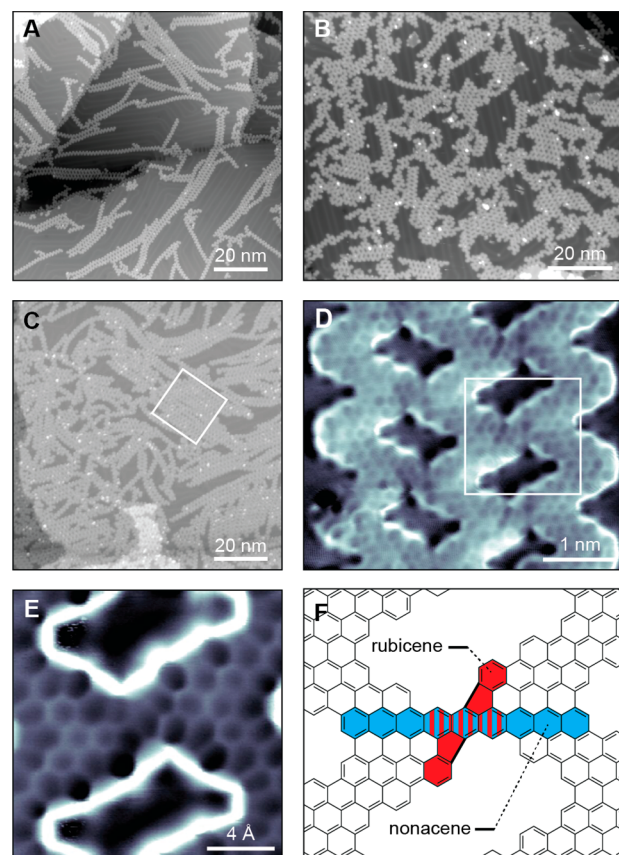
Scheme 1. Schematic Representation of the Bottom-up Synthesis of C-NPG from Molecular Precursors 1 and 2 (*anti* Configuration)

Figure 1. Synthesis of C-NPG. (A) STM topographic image of 0.25 monolayer coverage of C-NPG on Au(111) after deposition of **2** onto Au(111) held at $T_1 = 180$ °C and subsequent annealing to $T_2 = 400$ °C ($V = 1.2$ V, $I = 50$ pA). (B) STM topographic image of 0.75 monolayer coverage of C-NPG on Au(111) after deposition of **1** onto Au(111) held at 24 °C and subsequent annealing to $T_2 = 400$ °C ($V = -1.2$ V, $I = 50$ pA). (C) STM topographic image of 0.75 monolayer coverage of C-NPG on Au(111) after deposition of **2** onto Au(111) held at $T_1 = 180$ °C and subsequent annealing to $T_2 = 400$ °C ($V = 1.2$ V, $I = 50$ pA). (D) Bond-resolved STM image of a region containing three fused ribbons ($V = -50$ mV, $I = 200$ pA, $V_{osc} = 15$ mV, $f = 620$ Hz). (E) High-resolution bond-resolved STM image of the region indicated in (D) ($V = 20$ mV, $I = 250$ pA, $V_{osc} = 10$ mV, $f = 620$ Hz). (F) Schematic representation of the rubicene-type interface imaged in panels D and E.

to that of the C_{aryl}–H bond cleaved during the thermally induced cyclodehydrogenation of the GNR backbone.[15] The geometry of these chevron-type precursors defines the pore shape and size, whereas the reactivity of the cross-linking handles allows for the formation of benzene-fused linkages and facilitates two-dimensional extension of the structure. Our approach is high-yielding and selectively produces rubicene-type interfaces (highlighted in red in Scheme 1) by laterally fusing benzene rings through five-membered rings along either side of an extended acene. The resulting NPG features interface-localized frontier electronic states that emerge upon formation of these interfaces. The emergence of these states can be understood as linear combinations of molecular orbitals localized on the five-membered rings lining the edges of fluorene-chevron GNRs that couple into a two-dimensional (2D) superlattice geometry. We have experimentally characterized these electronic features using STS for both the final fused 2D nanopore states as well as isolated five-membered ring-localized states in 1D fluorene-chevron GNRs. The novel cross-linking handle utilized here represents progress toward creating electronically useful NPG, thus opening the door to exploring its potential in nanosieving and semiconductor device applications.

■ RESULTS AND DISCUSSION

The structures of molecular precursors **1** and **2** functionalized, respectively, with methyl and methylene cross-linking handles are depicted in Scheme 1. Deposition of precursors **1** or **2** onto a Au(111) surface held at $T_1 = 180$ °C and subsequent annealing to $T_2 = 400$ °C yields two-dimensionally extended chevron-type nanoporous graphene (C-NPG). Figure 1A shows that for an initial 0.25 monolayer coverage of **1**, a vast majority of the starting material forms cross-linked C-NPG

with some areas reaching 7 ribbons in width. Depositing 0.75 monolayer coverage of **2** onto a Au(111) surface held at 22 °C followed by annealing to $T_2 = 400$ °C results in a denser coverage of smaller C-NPG patches, as shown in Figure 1B. Here, close to 100% of structures on the surface are cross-linked, with several interconnected patches of roughly 10 × 10 nm in size. Long-range order, however, is diminished in comparison to the hot substrate deposition experiments. High quality samples of C-NPG are achieved by depositing 0.75 monolayer of **2** onto Au(111) held at $T_1 = 180$ °C, as shown in Figure 1C. Areas larger than 20 × 20 nm (white square in Figure 1C) and as wide as 40 nm in the lateral cross-link direction are observed. We attribute the high yield of the cross-linking reaction at $T_2 = 400$ °C to the similar activation energies required for homolytic C–H bond dissociation of the fluorenyl methylene groups and the barrier associated with cyclodehydrogenation of the GNR backbone.[15] We observe no significant difference between the two molecular precursors
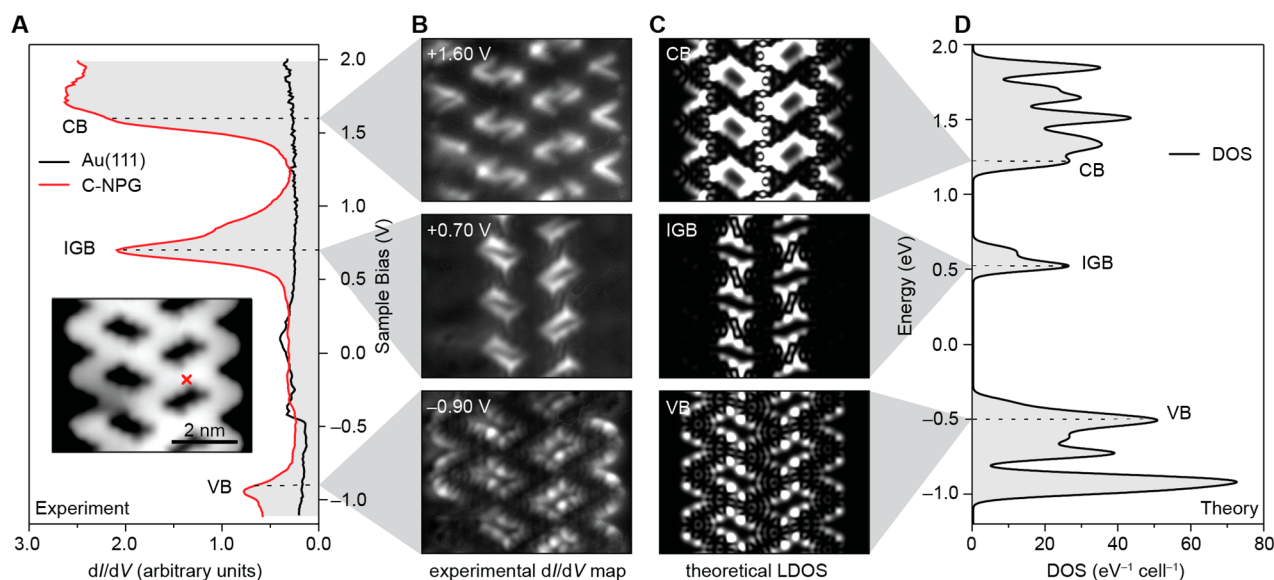
Figure 2. Electronic structure of the C-NPG. (A) STS dI/dV spectrum recorded on the rubicene interface of C-NPG. The inset shows a constant current STM topograph ($V = 0.7$ V, $I = 50$ pA) with the point spectroscopy location marked by a red cross (same region of C-NPG as shown in Figure 1D). (B) Differential conductance maps of VB (−0.90 V), IGB (0.72 V), and CB (1.60 V). (C) DFT simulated LDOS maps of the structure shown in the inset of panel A. The maps are calculated by integration over an energy window of 10 meV from the band edge. (D) DFT simulated density of states.

with regard to the ultimate product, although **2** shows a higher tendency to preorganize in the polymer phase, possibly due to π-stacking interactions between the fluorenyl groups of neighboring units, as shown in Figure S1. Although only Au(111) was used in the current work, in light of the successful synthesis of chevron-type GNRs on Cu(111), it is not inconceivable that other coinage metal surfaces could be used in the future for the synthesis of C-NPG.[16]

To resolve the atomic structure of this C-NPG, we performed bond-resolved scanning tunneling microscopy (BRSTM) using a carbon monoxide-passivated tip.[17−19] Figure 1D shows the BRSTM image of three interconnected ribbons over a 4 × 4 nm area. The ribbons are fused by rubicene-type linkages giving rise to a nanoporous structure containing parallelogram-shaped pores that are ∼0.5 nm wide in the short direction and ∼1 nm wide in the long direction. The orientation of the pores shown in Figure 1D alternates, resulting in a herringbone pattern with a unit cell that has screw symmetry in the ribbon axis. In the following discussion this lateral fusion pattern will be referred to as *anti*. An alternative coupling yielding aligned pores with inversion symmetry points in the ribbon axis will be referred to as *syn* (Figure S2). A higher-resolution BRSTM image around one of the interfaces in the *anti* configuration (Figure 1E) provides unambiguous assignment of the covalent bond structure of the lateral fusion product leading to C-NPG. The interface originates from a cross-dehydrogenative coupling that leads to the formation of two new C−C bonds that define the central benzene ring of the rubicene core (highlighted in red in Figure 1F). Another motif that emerges from the lateral fusion is a nonacene core where the newly created benzene ring represents the central ring (highlighted in blue in Figure 1F).[20] The fusion process ensures that carbon atoms at the apexes of the five-membered rings adopt a trigonal planar conformation, thus contributing a singly occupied p-orbital to the aromatic framework.

Having established the chemical structure of the C-NPG, we shift our focus to its electronic structure. Because the C-NPG is laterally fused through an extended acene, the electronic coupling between neighboring nanoribbons can be expected to be large. In addition, rubicene is known to be an electron acceptor and so it is reasonable to expect C-NPG to exhibit accessible frontier states.[21] We used scanning tunneling spectroscopy (STS) to verify these hypotheses, as shown below.

Figure 2A shows the energy-dependent local density of states (LDOS) recorded by measuring the differential conductance (dI/dV) of the STM tunnel junction while holding the tip above the interface region of the C-NPG shown in the inset (position indicated by red cross). Valence band (VB) and conduction band (CB) onsets are observed at −0.9 and 1.6 V, respectively, reflecting a bulk GNR band gap of 2.7 eV (similar to previously measured values for chevron GNRs on Au(111)).[17,22−24] A pronounced resonance, however, is observed at 0.72 V that has a distinct shoulder at higher bias. Because this resonance lies inside the bulk chevron GNR energy gap, we herein refer to this new feature as the in-gap band (IGB). Figure 2B shows energy-resolved dI/dV maps corresponding to the LDOS of the CB onset, the 0.72 V resonance feature, and the VB onset (top to bottom). We observe that the electronic wave functions corresponding to the band onsets are delocalized over the entire structure (i.e., all interfaces and edges light up) whereas the 0.72 V feature is localized exclusively at the pore interfaces.

The resonances observed in the dI/dV point spectra and the patterns observed in dI/dV mapping can be reasonably reproduced by *ab initio* electronic structure calculations. Figure 2D shows the C-NPG density of states (DOS) calculated using density functional theory (DFT), while Figure 2C shows the calculated LDOS maps corresponding to the CB onset, the IGB, and the VB onset for three fused ribbons having the same geometry, as seen experimentally. The theoretical bulk CB and VB band edge states extend throughout the C-NPG structure,
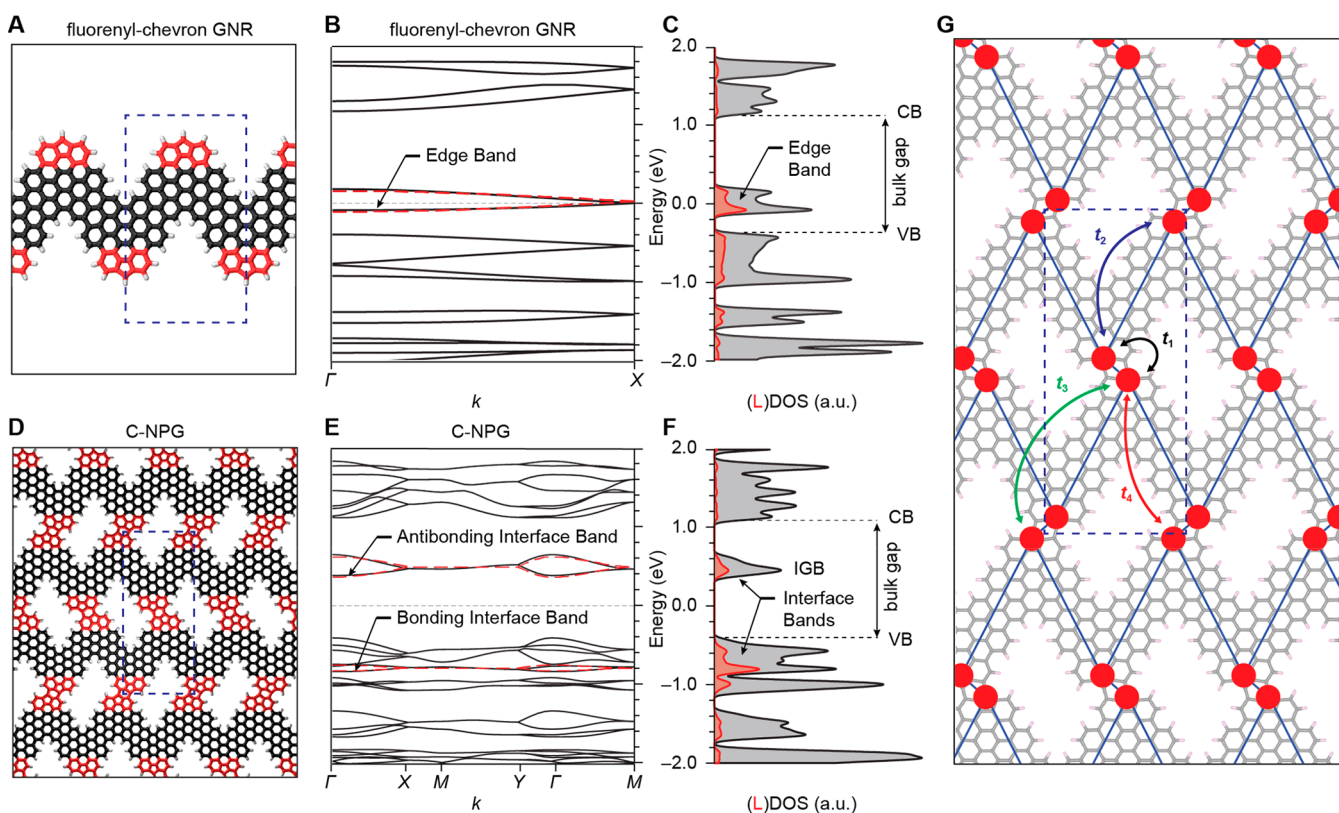
Figure 3. Electronic structure of the 1D fluorenyl-chevron GNR and 2D C-NPG. (A) Structure of an isolated fluorenyl-chevron GNR with the edge fluorenyl groups highlighted in red and the quasi 1D unit cell indicated by a rectangle. (B) Electronic dispersion of fluorenyl-chevron GNR. The black bands are predicted by DFT calculations, while the red dashed bands are those of an effective tight-binding model (with parameters fit to DFT results) described in the text. (C) Local (red) and total (black) density of states (200 k-points in the Brillouin zone) of fluorene-chevron GNR. (The local density of states is obtained by projecting states onto the π-orbitals of the fluorenyl groups.) (D) Structure of the C-NPG *anti* configuration with the interface (rubicene) groups highlighted in red and the 2D unit cell indicated by a rectangle. (E) Electronic dispersion of C-NPG. The black bands are the DFT result, while the red dashed bands are those of an effective tight-binding model (with parameter fit to DFT results) described in the text. (F) Local (red) and total (black) density of states (20 by 46 k-points) of C-NPG. (The local density of states is obtained by projection onto the π-orbitals in the pentagon region.) (G) Effective tight-binding model using basis states that represent the fluorenyl groups (red circles) coupled via nearest neighbor electronic hopping parameters t_1 (black) and t_2 (blue) and next-nearest-neighbor hopping parameters t_3 and t_4 (green and red, respectively).

whereas the calculated IGB localizes at the pore interfaces with small wave function overlap with neighboring pores, in good agreement with experiment. The peak shape of the IGB, including the distinct high-energy shoulder, is also accurately reproduced by the calculation. These results demonstrate that C-NPG is a new 2D electronic material with low-energy electronic states deep within the bulk band gap of the constituent GNRs that are primarily localized on the rubicene interfaces adjacent to pores. Furthermore, even though a defect is clearly present in the bottom-left corner, the electronic structure remains unaffected, with the IGB uniformly distributed over the interfaces, in good accordance with theory.

Because the interfaces define a superlattice, it is expected that the electronic states localized on them should give rise to 2D dispersing features in the C-NPG band structure.[25−32] It is useful to analyze this interface behavior in more depth to gain insight into how to tune the electronic structure of NPG. This is not only relevant to the specific C-NPG synthesized here, but in general to other possible C-NPG varieties that may be designed through functional analogues of monomers **1** and **2**.

We start by considering a hypothetical isolated fluorenyl-chevron GNR exhibiting evenly spaced sp²-hybridized π-radicals at the apexes of fluorenyl groups lining both edges of the ribbon (Figure 3A). This structure was chosen as a C-NPG

building block because the fluorenyl groups along the edges (highlighted in red) constitute one-half of the rubicene interface structure found in C-NPG. Furthermore, this structure represents the GNR expected to arise from precursors **1** and **2** (other possible structures, e.g. fluorenylidene edges (Figure 4C), gave similar results). Figure 3B shows the DFT calculated band structure of this GNR while Figure 3C shows the local (red) and total (black) DOS (the LDOS here is obtained by projecting band states onto the fluorenyl groups highlighted in red in Figure 3A). The 1D GNR band structure shows bulk VB and CB band edges as well as an IGB. The projected LDOS (Figure 3C) indicates that the IGB arises from atoms lining the convex edge of fluorenyl-chevron GNRs. A significant difference between this isolated GNR and C-NPG is that the isolated GNR is metallic due to the in-gap band straddling the Fermi level.[33]

The semiconducting band structure of 2D C-NPG (shown in Figure 3E), by contrast, shows a higher energy IGB that lies ∼0.5 eV above the Fermi level. Close inspection shows another difference between the 2D C-NPG DOS (Figure 3F) and the isolated 1D GNR DOS (Figure 3C): the localized interface states for C-NPG appear at *two energies*, not just one. One band of states is the familiar IGB above the Fermi energy, but the other occurs much lower in energy and appears below the
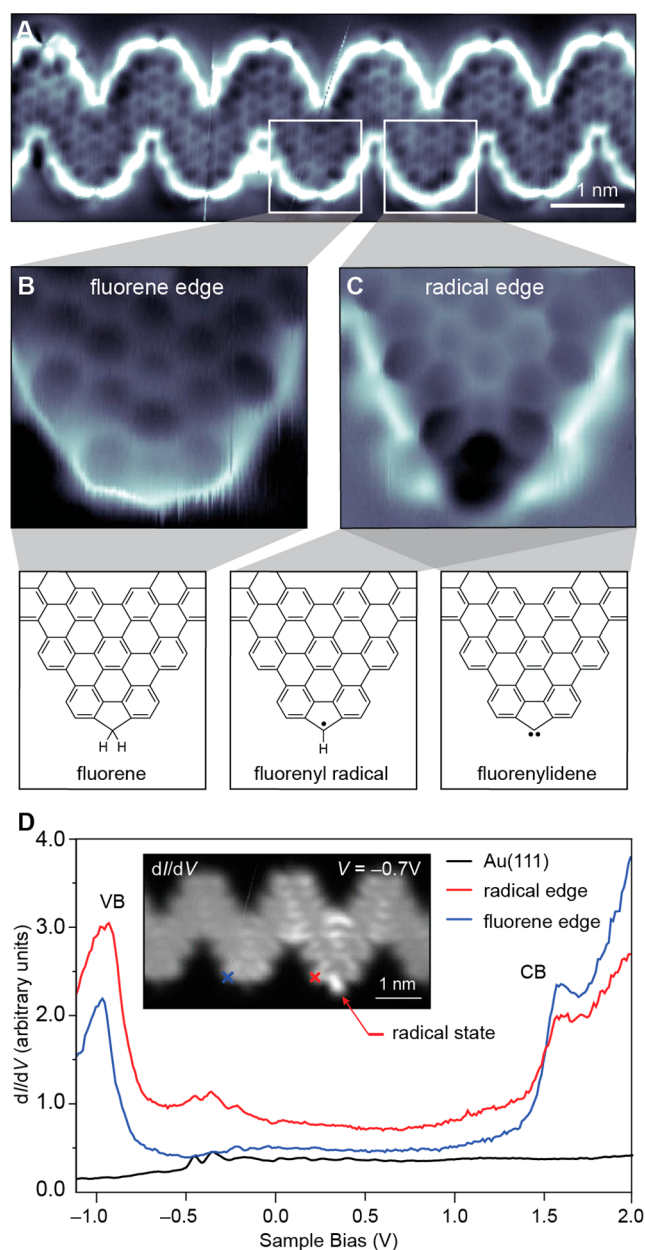
Figure 4. Edge electronic structure of isolated fluorene-chevron GNR. (A) Bond-resolved STM image of an isolated fluorene-chevron GNR using CO-tip ($V = -50$ mV, $I = 180$ pA, $V_{osc} = 20$ mV). (B) Bond-resolved STM image of the segment indicated in (A) containing a methylene edge group ($V = 15$ mV, $I = 200$ pA, $V_{osc} = 10$ mV). (C) Bond-resolved STM image of the neighboring segment indicated in (A) ($V = 20$ mV, $I = 250$ pA, $V_{osc} = 10$ mV). Possible chemical structures are depicted below. (D) Scanning tunneling spectroscopy of an isolated fluorene-chevron GNR ($V_{osc} = 4$ mV, $f = 620$ Hz). The red and blue spectra are recorded at the positions indicated in the inset ($V_{osc} = 20$ mV, $f = 620$ Hz). The inset shows a constant height dI/dV scan of the GNR obtained at $V = -0.7$ V for the same nanoribbon shown in panel A. Location of the radical state is marked by an arrow (same edge element as shown in panel C).

VB edge. Formation of C-NPG is thus seen to cause the edge states of isolated GNRs (Figure 3B, C) to split to yield two sets of C-NPG interface bands. Here, fusion of each fluorenyl pair shared between adjacent GNRs into a single rubicene moiety causes the fluorenyl orbitals to hybridize and split energetically into bonding/antibonding pairs. The antibonding states

combine to form the C-NPG IGB at higher energy, while the bonding states form the lower energy C-NPG band. This picture is supported by analysis of the wave functions, where the bonding (antibonding) 2D interface states can be recognized as an antisymmetric (symmetric) combination of 1D edge states (see Figure S3). Edge hybridization thus causes what would otherwise be isolated 1D metallic GNRs to evolve (at least conceptually) into a semiconducting 2D nanopore mesh.

These *ab initio* DFT electronic structure results can be more intuitively understood using an effective tight-binding model. Here we consider the edge orbitals localized on the fluorenyl groups as effective basis states that link up to form a 1D electronic network for the isolated GNR (Figure 3A) and a 2D electronic network for the C-NPG (as shown by the red circles in Figure 3G). In the 1D case, the electronic dispersion can be found by assuming that an electron placed on one edge orbital has an amplitude t_2 to hop along the ribbon to an adjacent orbital. In the 2D case, the edge orbital network has an even stronger coupling t_1 between edge orbitals within a single rubicene moiety that is responsible for splitting them into bonding and antibonding interface states (weaker next-nearest-neighbor coupling is described by hopping amplitudes t_3 and t_4). The 1D GNR thus has two basis states per unit cell with one hopping parameter t_2, and so results in two bands that fit well to the GNR DFT band structure for $t_2 = -65$ meV, as shown by the two dashed lines in Figure 3B. The 2D C-NPG, on the other hand, has four basis states per unit cell which result in four bands as shown by the dashed lines in Figure 3E. These bands fit well to the interface bands of the 2D C-NPG DFT band structure after optimization of the hopping amplitudes ($t_1 = 645$ meV, $t_2 = -23$ meV, $t_3 = -22$ meV, $t_4 = -20$ meV). These interface states form a distorted honeycomb lattice with distinct hopping parameters compared to a normal graphene lattice. The C-NPG bands are split into an upper pair that lie in the bulk gap and a lower pair that are resonant with the valence band complex. These are precisely the bands that arise from hybridization-induced splitting of orbitals or modes localized in the fluorenyl edge groups of the isolated GNR in Figure 3A–C. The electronic behavior of the 2D C-NPG pore states is thus encoded in the edge-states engineered for the constituent 1D building block GNRs through rational design of the molecular precursor.

A remaining question is whether the C-NPG GNR building block, the fluorenyl-chevron GNR shown in Figure 3A, can actually exist in a laboratory rather than simply being a useful construct for understanding C-NPG electronic structure. The answer here is mixed. We do observe isolated, unlinked GNRs in lower-coverage samples, but their structure is not identical to Figure 3A. A typical example is shown in Figure 4A which shows a BRSTM image of an isolated GNR derived from precursor 1 (a standard STM topograph of this GNR can be seen in Figure S4B). Close-up images of the edges of this GNR in Figures 4B and 4C show two different edge structures (other types are also possible, see Figure S4). The edge structure shown in Figure 4B features a hydrogen-saturated five-membered ring within a fluorene group and is by far the dominant edge structure (80% of edge segments). The edge structure in Figure 4C is seen much less frequently (5% percent of edge segments) but is highly reproducible. The apex of the edge structure in Figure 4C extends further than the edge structure in Figure 4B and also appears to be pulled closer

to the surface (i.e., it has darker contrast in the BRSTM image).

STM spectroscopy helps us to better understand the nature of these different GNR edge structures. Figure 4D shows a dI/dV spectrum (blue curve) obtained with the STM tip held over the dominant edge structure shown in Figure 4B. Valence and conduction band peaks are clearly visible and result in a bandgap of 2.4 eV, consistent with previous spectroscopy of conventional chevron GNRs lacking the five-membered ring of the fluorenyl group.[17,22,23] No signs of in-gap states are seen for this edge structure. Spectroscopy performed on edge structures like that shown in Figure 4C, on the other hand, are different, as shown by the red curve in Figure 4D. Here, the VB and CB features are seen as before, but a new in-gap feature also arises, a broad peak centered at approximately −0.4 V that is not seen for the more common edge structure of Figure 4B. The spatial extent of this new electronic feature can be seen in the dI/dV image of Figure 4D (inset) obtained at −0.7 V. Here, edge groups having an appearance like the structure in Figure 4B are featureless, while an edge group equivalent to that in Figure 4C (arrow) has a prominent protrusion at the apex that lights up at this energy.

This behavior is explained by the presence of methylene (CH$_2$) groups at the common apex structure shown in Figure 4B. Here, hydrogen passivation removes the fluorenyl radical state by rehybridization of the apical carbon atom into the tetrahedral methylene group in fluorene, thus excluding it from interaction with the π-system.[15,34−36] This explains why spectroscopy of the fluorene edge structure shows the same behavior as conventional chevron GNRs which lack the apical carbon atom of fluorene-chevron GNRs. The edge structure of Figure 4C, on the other hand, is consistent with an sp^2-hybridized π-radical obtained from spurious dehydrogenation of a fluorene group (e.g., a fluorenyl radical or fluorenylidene as depicted in Figure 4C). This is consistent with on-surface dehydrogenation in cyclopentadiene moieties which has been shown to compete with methylene-directed fusion and to result in highly reactive carbene or methyne groups.[15,36] Stabilization of these intermediate radical species by the surface explains the dark contrast in the BRSTM image, as well as the broadness of the in-gap resonance (due to strong coupling with the underlying Au(111) surface).[37] The edge motif of Figure 4C thus exhibits the type of radical behavior that can be viewed as the basis of C-NPG electronic structure.

CONCLUSION

Depositing methyl and methylene bearing precursors **1** or **2** onto a Au(111) substrate and annealing to 400 °C yields two-dimensionally extended C-NPG. This new 2D material emerges due to the reactivity of methyl and methylene cross-linking handles toward cross-dehydrogenative coupling at low temperatures. Bond-resolved scanning tunneling microscopy reveals that internal interfaces within this 2D pore network exhibit rubicene-type linkers that arise from the lateral fusion of partially dehydrogenated fluorene-chevron GNRs. The resulting C-NPG exhibits a novel in-gap band localized on the rubicene interfaces around the pores. These features are reproduced by both DFT and coarse-grained tight-binding calculations which show that the electronic structure of this new 2D material may be understood in terms of the edge modes of 1D GNR building blocks. The fully linked 2D behavior is also consistent with the experimental properties of isolated GNRs where sp^2-hybridized π-radicals exist due to

spurious dehydrogenation of the fluorenyl groups lining the edge. The cross-linking handles can be incorporated in a wide variety of molecular precursors, thus paving the way toward nanoporous graphenes with variable pore density and morphology. The control and incorporation of π-radical states into 2D porous graphene topologies opens exciting new possibilities for exploring tunable pore networks in the future.

■ EXPERIMENTAL SECTION

Materials and General Methods. Unless otherwise stated, all manipulations of air- and/or moisture-sensitive compounds were carried out in oven-dried glassware under an atmosphere of N$_2$. All solvents and reagents were purchased from Alfa Aesar, Spectrum Chemicals, Acros Organics, TCI America, and Sigma-Aldrich and were used as received unless otherwise noted. Organic solvents were dried by passing through a column of alumina and degassed by vigorous bubbling of N$_2$ or Ar through the solvent for 20 min. Flash column chromatography was performed on SiliCycle silica gel (particle size 40−63 μm). Thin layer chromatography was performed using SiliCycle silica gel 60 Å F-254 precoated plates (0.25 mm thick) and visualized by UV absorption. All ^{1}H and ^{13}C {^{1}H} NMR spectra were recorded on Bruker AV-400 and AV-600 MHz spectrometers, and are referenced to residual solvent peaks (CDCl$_3$ ^{1}H NMR = 7.26 ppm, ^{13}C NMR = 77.16 ppm; C$_6$D$_6$ ^{1}H NMR δ 7.16 ppm, ^{13}C NMR δ 128.06 ppm; CD$_2$Cl$_2$ ^{1}H NMR = 5.32 ppm, ^{13}C NMR = 53.48 ppm). ESI mass spectrometry was performed on a Finnigan LTQFT (Thermo) spectrometer. MALDI mass spectrometry was performed on a Voyager-DE PRO (Applied Biosystems Voyager System 6322) in positive mode using a matrix of dithranol.

6,11-Dibromo-2-(6-methyl-[1,1′-biphenyl]-2-yl)-1,4-diphenyltriphenylene (1). A 5 mL Schlenk tube was charged under N$_2$ with 5,10-dibromo-1,3-diphenyl-2H-cyclopenta[l]phenanthren-2-one (0.184 g, 0.34 mmol) and 2-ethynyl-6-methyl-1,1′-biphenyl (0.065 g, 0.34 mmol) in degassed *o*-xylene (2 mL). The reaction mixture was sealed under N$_2$ and stirred for 18 h at 145 °C. The reaction mixture was cooled to 24 °C and concentrated on a rotary evaporator. Column chromatography (SiO$_2$; 3:1 hexane/CH$_2$Cl$_2$) yielded **1** (0.186 g, 0.26 mmol, 78%) as a colorless crystalline solid. ^{1}H NMR (600 MHz, CD$_2$Cl$_2$) δ 8.19 (dd, J = 14.5, 8.7 Hz, 2H), 7.69 (d, J = 2.0 Hz, 1H), 7.55−7.39 (m, 9H), 7.31−7.19 (m, 6H), 7.11−7.03 (m, 2H), 7.03−6.94 (m, 3H), 6.41 (s, 1H), 6.34 (s, 1H), 1.99 (s, 3H) ppm; ^{13}C {^{1}H} NMR (151 MHz, CDCl$_3$) δ = 143.7, 141.5, 141.0, 140.9, 140.4, 139.3, 137.8, 137.3, 136.4, 134.8, 133.4, 133.1, 132.8, 132.8, 131.9, 131.6, 131.1, 130.6, 130.3, 129.8, 129.7, 129.6, 129.6, 129.5, 129.5, 129.5, 129.5, 129.4, 129.0, 128.6, 128.3, 127.8, 127.6, 127.4, 127.2, 126.7, 126.5, 124.7, 124.6, 120.2, 120.0, 21.4 ppm; HRMS (EI-TOF) *m/z*: [C$_{43}$H$_{28}$Br$_2$]$^+$ calcd [C$_{43}$H$_{28}$Br$_2$] 702.0558; found 702.0559.

6,11-Dibromo-2-(9H-fluoren-4-yl)-1,4-diphenyltriphenylene (2). A 10 mL Schlenk flask was charged with 4-(6,11-dibromo-1,4-diphenyltriphenylen-2-yl)-9H-fluoren-9-one (71.6 mg, 0.10 mmol), red phosphorus (21.1 mg, 0.68 mmol) and HI (0.28 mL, 57 wt %) in propionic acid (2 mL). The suspension was heated to 145 °C under N$_2$ for 18 h. The suspension was cooled to 24 °C and quenched with saturated aqueous K$_2$CO$_3$ solution. The suspension was washed three times with CH$_2$Cl$_2$. The combined organic phases were washed with saturated aqueous NaCl solution, dried over MgSO$_4$, and concentrated on a rotary evaporator. Column chromatography (SiO$_2$; 1:1 CH$_2$Cl$_2$/hexanes) yielded **2** (59.2 mg, 0.084 mmol, 84%) as a colorless solid. ^{1}H NMR (500 MHz, CD$_2$Cl$_2$) δ 8.28 (dd, J = 8.8, 3.7 Hz, 2H), 7.88 (d, J = 2.0 Hz, 1H), 7.71 (m, 2H), 7.58 (dd, J = 8.7, 2.0 Hz, 1H), 7.53−7.41 (m, 8H), 7.20−7.10 (m, 5H), 7.02−6.96 (m, 4H), 6.88 (d, J = 2.0 Hz, 1H), 3.91 (s, 2H) ppm; ^{13}C {^{1}H} NMR (151 MHz, CDCl$_3$) δ 143.6, 143.4, 143.2, 141.6, 140.9, 140.3, 139.4, 139.0, 137.6, 136.0, 133.0, 132.7, 132.7, 132.4, 131.7, 131.4, 131.1, 130.7, 129.8, 129.6, 129.5, 129.5, 129.3, 129.2, 129.1, 128.4, 128.2, 127.6, 127.0, 126.5, 126.3, 125.7, 124.7, 124.6, 124.5, 123.4, 122.6, 120.1, 120.0, 36.8 ppm; HRMS (ESI-TOF) *m/z*: [C$_{43}$H$_{25}$Br$_2$]$^−$ calcd [C$_{43}$H$_{25}$Br$_2$] 699.0328; found 699.0325.

Sample Preparation. Atomically clean Au(111) surfaces were prepared through repeated cycles of argon ion (Ar$^+$) bombardment and annealing. Deposition of **1** and **2** was achieved by sublimation using a home-built Knudsen cell evaporator at crucible temperatures of 200 °C. Polymerization, cyclodehydrogenation, and cross-dehydrogenative coupling were performed by ramping the surface temperature to 180 °C and then subsequently to 400 °C.

STM Measurements. All STM experiments were carried out using a commercial Createc LT-STM held at T = 4.5 K using platinum−iridium tips. Image processing of the STM scans was performed using WSxM software.[38] Scanning tunneling spectroscopy, differential conductance mapping, and bond-resolved STM experiments were performed with the use of a lock-in amplifier using a wiggle voltage (V_{osc}) of 4 to 20 mV at a frequency of f = 620 Hz.

Calculations. DFT calculations were performed using Quantum Espresso.[39] A 15 Å vacuum spacing in a supercell geometry is used along the nonperiodic (normal to the carbon plane in the case of C-NPG) directions of each material. The atomic geometry is fully relaxed until every component of the forces on each atom are smaller than 0.01 eV/Å. Scalar relativistic and norm-conserving pseudo potentials of C and H are used. The effective tight-binding fitting was done using a custom-built python code. For both DFT and tight-binding calculations, a 20 meV Lorentzian broadening was applied in the calculation of the (local) density of states.

■ ASSOCIATED CONTENT

ⓈⒾ Supporting Information

The Supporting Information is available free of charge at https://pubs.acs.org/doi/10.1021/jacs.0c05235.

> Figures S1−S4, methods and instrumentation, synthetic procedures for **1** and **2**, Schemes S1−S2, and NMR spectra (Figures S5−S12) (PDF)

■ AUTHOR INFORMATION

Corresponding Authors

Steven G. Louie − *Department of Physics, University of California, Berkeley, California 94720, United States; Materials Sciences Division, Lawrence Berkeley National Laboratory, Berkeley, California 94720, United States;* ◉ orcid.org/0000-0003-0622-0170; Email: sglouie@berkeley.edu

Michael F. Crommie − *Department of Physics, University of California, Berkeley, California 94720, United States; Materials Sciences Division, Lawrence Berkeley National Laboratory, Berkeley, California 94720, United States; Kavli Energy NanoSciences Institute at the University of California Berkeley and the Lawrence Berkeley National Laboratory, Berkeley, California 94720, United States;* Email: crommie@berkeley.edu

Felix R. Fischer − *Department of Chemistry, University of California, Berkeley, California 94720, United States; Materials Sciences Division, Lawrence Berkeley National Laboratory, Berkeley, California 94720, United States; Kavli Energy NanoSciences Institute at the University of California Berkeley and the Lawrence Berkeley National Laboratory, Berkeley, California 94720, United States;* ◉ orcid.org/0000-0003-4723-3111; Email: ffischer@berkeley.edu

Authors

Peter H. Jacobse − *Department of Physics, University of California, Berkeley, California 94720, United States;* ◉ orcid.org/0000-0001-7319-4836

Ryan D. McCurdy − *Department of Chemistry, University of California, Berkeley, California 94720, United States*

Jingwei Jiang − *Department of Physics, University of California, Berkeley, California 94720, United States*

Daniel J. Rizzo − *Department of Physics, University of California, Berkeley, California 94720, United States*

Gregory Veber − *Department of Chemistry, University of California, Berkeley, California 94720, United States*

Paul Butler − *Department of Physics, University of California, Berkeley, California 94720, United States*

Rafał Zuzak − *Department of Physics, University of California, Berkeley, California 94720, United States; Center for Nanometer-Scale Science and Advanced Materials, NANOSAM, Faculty of Physics, Astronomy and Applied Computer Science, Jagiellonian University, PL 30-348 Kraków, Poland*

Complete contact information is available at:
https://pubs.acs.org/10.1021/jacs.0c05235

Author Contributions

[⊥]P.H.J., R.D.M., and J.J. contributed equally.

Notes

The authors declare no competing financial interest.

■ ACKNOWLEDGMENTS

■ REFERENCES

(1) Surwade, S. P.; Smirnov, S. N.; Vlassiouk, I. V.; Unocic, R. R.; Veith, G. M.; Dai, S.; Mahurin, S. M. Water Desalination Using Nanoporous Single-Layer Graphene. *Nat. Nanotechnol.* **2015**, *10* (5), 459−464.

(2) Cohen-Tanugi, D.; Grossman, J. C. Water Desalination across Nanoporous Graphene. *Nano Lett.* **2012**, *12* (7), 3602−3608.

(3) Koenig, S. P.; Wang, L.; Pellegrino, J.; Bunch, J. S. Selective Molecular Sieving through Porous Graphene. *Nat. Nanotechnol.* **2012**, *7* (11), 728−732.

(4) Jiang, D. E.; Cooper, V. R.; Dai, S. Porous Graphene as the Ultimate Membrane for Gas Separation. *Nano Lett.* **2009**, *9* (12), 4019−4024.

(5) Rollings, R. C.; Kuan, A. T.; Golovchenko, J. A. Ion Selectivity of Graphene Nanopores. *Nat. Commun.* **2016**, *7* (1), 11408.

(6) Sint, K.; Wang, B.; Král, P. Selective Ion Passage through Functionalized Graphene Nanopores. *J. Am. Chem. Soc.* **2008**, *130* (49), 16448−16449.

(7) Garaj, S.; Hubbard, W.; Reina, A.; Kong, J.; Branton, D.; Golovchenko, J. A. Graphene as a Subnanometre Trans-Electrode Membrane. *Nature* **2010**, *467* (7312), 190−193.

(8) Venkatesan, B. M.; Bashir, R. Nanopore Sensors for Nucleic Acid Analysis. *Nat. Nanotechnol.* **2011**, *6* (10), 615−624.

(9) Traversi, F.; Raillon, C.; Benameur, S. M.; Liu, K.; Khlybov, S.; Tosun, M.; Krasnozhon, D.; Kis, A.; Radenovic, A. Detecting the

Translocation of DNA through a Nanopore using Graphene Nanoribbons. *Nat. Nanotechnol.* **2013**, *8* (12), 939−945.

(10) Dontschuk, N.; Stacey, A.; Tadich, A.; Rietwyk, K. J.; Schenk, A.; Edmonds, M. T.; Shimoni, O.; Pakes, C. I.; Prawer, S.; Cervenka, J. A graphene field-effect transistor as a molecule-specific probe of DNA nucleobases. *Nat. Commun.* **2015**, *6* (1), 6563.

(11) Moreno, C.; Vilas-Varela, M.; Kretz, B.; Garcia-Lekue, A.; Costache, M. V.; Paradinas, M.; Panighel, M.; Ceballos, G.; Valenzuela, S. O.; Peña, D.; Mugarza, A. Bottom-up Synthesis of Multifunctional Nanoporous Graphene. *Science* **2018**, *360* (6385), 199−203.

(12) Shekhirev, M.; Zahl, P.; Sinitskii, A. Phenyl Functionalization of Atomically Precise Graphene Nanoribbons for Engineering Inter-Ribbon Interactions and Graphene Nanopores. *ACS Nano* **2018**, *12* (8), 8662−8669.

(13) Teeter, J. D.; Costa, P. S.; Zahl, P.; Vo, T. H.; Shekhirev, M.; Xu, W.; Zeng, X. C.; Enders, A.; Sinitskii, A. Dense Monolayer Films of Atomically Precise Graphene Nanoribbons on Metallic Substrates Enabled by Direct Contact Transfer of Molecular Precursors. *Nanoscale* **2017**, *9* (47), 18835−18844.

(14) Sinitskii, A. A Recipe for Nanoporous Graphene. *Science* **2018**, *360* (6385), 154−155.

(15) Di Giovannantonio, M.; Eimre, K.; Yakutovich, A. V.; Chen, Q.; Mishra, S.; Urgel, J. I.; Pignedoli, C. A.; Ruffieux, P.; Müllen, K.; Narita, A.; Fasel, R. On-Surface Synthesis of Antiaromatic and Open-Shell Indeno[2,1-b]Fluorene Polymers and Their Lateral Fusion into Porous Ribbons. *J. Am. Chem. Soc.* **2019**, *141* (31), 12346−12354.

(16) Teeter, J. D.; Costa, P. S.; Mehdi Pour, M.; Miller, D. P.; Zurek, E.; Enders, A.; Sinitskii, A. Epitaxial Growth of Aligned Atomically Precise Chevron Graphene Nanoribbons on Cu(111). *Chem. Commun.* **2017**, *53* (60), 8463−8466.

(17) Nguyen, G. D.; Tsai, H. Z.; Omrani, A. A.; Marangoni, T.; Wu, M.; Rizzo, D. J.; Rodgers, G. F.; Cloke, R. R.; Durr, R. A.; Sakai, Y.; Liou, F.; Aikawa, A. S.; Chelikowsky, J. R.; Louie, S. G.; Fischer, F. R.; Crommie, M. F. Atomically Precise Graphene Nanoribbon Heterojunctions from a Single Molecular Precursor. *Nat. Nanotechnol.* **2017**, *12* (11), 1077−1082.

(18) Gross, L.; Mohn, F.; Moll, N.; Liljeroth, P.; Meyer, G. The Chemical Structure of a Molecule Resolved by Atomic Force Microscopy. *Science* **2009**, *325* (5944), 1110−1114.

(19) Bartels, L.; Meyer, G.; Rieder, K.-H. Controlled Vertical Manipulation of Single CO Molecules with the Scanning Tunneling Microscope: A Route to Chemical Contrast. *Appl. Phys. Lett.* **1997**, *71* (2), 213−215.

(20) Zuzak, R.; Dorel, R.; Krawiec, M.; Such, B.; Kolmer, M.; Szymonski, M.; Echavarren, A. M.; Godlewski, S. Nonacene Generated by On-Surface Dehydrogenation. *ACS Nano* **2017**, *11* (9), 9321−9329.

(21) Chen, H.-Y.; Golder, J.; Yeh, S.-C.; Lin, C.-W.; Chen, C.-T.; Chen, C.-T. Diindeno[1,2-g:1′,2′-s]Rubicene: All-Carbon Non-Full-erene Electron Acceptor for Efficient Bulk-Heterojunction Organic Solar Cells with High Open-Circuit Voltage. *RSC Adv.* **2015**, *5* (5), 3381−3385.

(22) Cai, J.; Pignedoli, C. A.; Talirz, L.; Ruffieux, P.; Söde, H.; Liang, L.; Meunier, V.; Berger, R.; Li, R.; Feng, X.; Müllen, K.; Fasel, R. Graphene Nanoribbon Heterojunctions. *Nat. Nanotechnol.* **2014**, *9* (11), 896−900.

(23) Wang, S.; Wang, J. Quasiparticle Energies and Optical Excitations in Chevron-Type Graphene Nanoribbon. *J. Phys. Chem. C* **2012**, *116* (18), 10193−10197.

(24) Rizzo, D. J.; Wu, M.; Tsai, H.-Z.; Marangoni, T.; Durr, R. A.; Omrani, A. A.; Liou, F.; Bronner, C.; Joshi, T.; Nguyen, G. D.; Rodgers, G. F.; Choi, W.-W.; Jørgensen, J. H.; Fischer, F. R.; Louie, S. G.; Crommie, M. F. Length-Dependent Evolution of Type II Heterojunctions in Bottom-Up-Synthesized Graphene Nanoribbons. *Nano Lett.* **2019**, *19* (5), 3221−3228.

(25) Sevinçli, H.; Topsakal, M.; Ciraci, S. Superlattice Structures of Graphene-Based Armchair Nanoribbons. *Phys. Rev. B: Condens. Matter Mater. Phys.* **2008**, *78* (24), 245402.

(26) Topsakal, M.; Sevinçli, H.; Ciraci, S. Spin Confinement in the Superlattices of Graphene Ribbons. *Appl. Phys. Lett.* **2008**, *92* (17), 173118.

(27) Liang, X.; Jung, Y. S.; Wu, S.; Ismach, A.; Olynick, D. L.; Cabrini, S.; Bokor, J. Formation of Bandgap and Subbands in Graphene Nanomeshes with Sub-10 Nm Ribbon Width Fabricated via Nanoimprint Lithography. *Nano Lett.* **2010**, *10* (7), 2454−2460.

(28) Zamani, S.; Farghadan, R. Graphene Nanoribbon Spin-Photodetector. *Phys. Rev. Appl.* **2018**, *10* (3), 34059.

(29) Cao, T.; Zhao, F.; Louie, S. G. Topological Phases in Graphene Nanoribbons: Junction States, Spin Centers, and Quantum Spin Chains. *Phys. Rev. Lett.* **2017**, *119* (7), 1−5.

(30) Jiang, J.; Louie, S. G. Topology Classification from Chiral Symmetry: Chiral Phase Index and Spin Correlations in Graphene Nanoribbons. 2020. https://arxiv.org/abs/2002.04628

(31) Rizzo, D. J.; Veber, G.; Cao, T.; Bronner, C.; Chen, T.; Zhao, F.; Rodriguez, H.; Louie, S. G.; Crommie, M. F.; Fischer, F. R. Topological Band Engineering of Graphene Nanoribbons. *Nature* **2018**, *560* (7717), 204−208.

(32) Gröning, O.; Wang, S.; Yao, X.; Pignedoli, C. A.; Borin Barin, G.; Daniels, C.; Cupo, A.; Meunier, V.; Feng, X.; Narita, A.; Müllen, K.; Ruffieux, P.; Fasel, R. Engineering of Robust Topological Quantum Phases in Graphene Nanoribbons. *Nature* **2018**, *560*, 209.

(33) Rizzo, D. J.; Veber, G.; Jiang, J.; Mccurdy, R.; Cao, T.; Chen, T.; Louie, S. G.; Fischer, F. R.; Crommie, M. F. Inducing Metallicity in Graphene Nanoribbons via Zero-Mode Superlattices. 2019. https://arxiv.org/abs/1911.00601.

(34) Talirz, L.; Söde, H.; Cai, J.; Ruffieux, P.; Blankenburg, S.; Jafaar, R.; Berger, R.; Feng, X.; Müllen, K.; Passerone, D.; Fasel, R.; Pignedoli, C. A. Termini of Bottom-Up Fabricated Graphene Nanoribbons. *J. Am. Chem. Soc.* **2013**, *135* (6), 2060−2063.

(35) Ijäs, M.; Ervasti, M.; Uppstu, A.; Liljeroth, P.; van der Lit, J.; Swart, I.; Harju, A. Electronic States in Finite Graphene Nanoribbons: Effect of Charging and Defects. *Phys. Rev. B: Condens. Matter Mater. Phys.* **2013**, *88* (7), 75429.

(36) Di Giovannantonio, M.; Urgel, J. I.; Beser, U.; Yakutovich, A. V.; Wilhelm, J.; Pignedoli, C. A.; Ruffieux, P.; Narita, A.; Müllen, K.; Fasel, R. On-Surface Synthesis of Indenofluorene Polymers by Oxidative Five-Membered Ring Formation. *J. Am. Chem. Soc.* **2018**, *140* (10), 3532−3536.

(37) van der Lit, J.; Boneschanscher, M. P.; Vanmaekelbergh, D.; Ijäs, M.; Uppstu, A.; Ervasti, M.; Harju, A.; Liljeroth, P.; Swart, I. Suppression of Electron−Vibron Coupling in Graphene Nanoribbons Contacted via a Single Atom. *Nat. Commun.* **2013**, *4* (1), 2023.

(38) Horcas, I.; Fernández, R.; Gómez-Rodríguez, J. M.; Colchero, J.; Gómez-Herrero, J.; Baro, A. M. WSXM: A Software for Scanning Probe Microscopy and a Tool for Nanotechnology. *Rev. Sci. Instrum.* **2007**, *78* (1), 13705.

(39) Giannozzi, P.; Baroni, S.; Bonini, N.; Calandra, M.; Car, R.; Cavazzoni, C.; Ceresoli, D.; Chiarotti, G. L.; Cococcioni, M.; Dabo, I.; Dal Corso, A.; de Gironcoli, S.; Fabris, S.; Fratesi, G.; Gebauer, R.; Gerstmann, U.; Gougoussis, C.; Kokalj, A.; Lazzeri, M.; Martin-Samos, L.; Marzari, N.; Mauri, F.; Mazzarello, R.; Paolini, S.; Pasquarello, A.; Paulatto, L.; Sbraccia, C.; Scandolo, S.; Sclauzero, G.; Seitsonen, A. P.; Smogunov, A.; Umari, P.; Wentzcovitch, R. M. Quantum ESPRESSO: a modular and open-source software project for quantum simulations of materials. *J. Phys.: Condens. Matter* **2009**, *21*, 395502.